Materials Advances

Accepted Manuscript

This article can be cited before page numbers have been issued, to do this please use: T. Nazir, Q. Abbas, S. M. T. Kazmi, C. Li, X. Xu and M. A. Rafiq, *Mater. Adv.*, 2026, DOI: 10.1039/D5MA01527H.

ROYAL SOCIETY OF CHEMISTRY

rsc.li/materials-advances

Extraction of Schottky Diode parameters, Electron Transport and Dielectric Relaxation in $PdSe_2$ nanoflake

View Article Online
DOI: 10.1039/D5MA01527H

Tooba Nazir[a], Qaisar Abbas[a,b], Syed Mesam Tamar Kazmi[a,b], Chuanbo Li[c], Xiulai Xu[d,e], M. A. Rafiq*[,b,f]

[a]*Department of Physics and Applied Mathematics, Pakistan Institute of Engineering and Applied Sciences, PO Nilore, Islamabad, 45650 Pakistan.*
[b]*Condensed Matter Physics Laboratories, Center for Mathematical Sciences, PIEAS, Islamabad, 45650 Pakistan.*
[c]*School of Science, Minzu University of China, Beijing 100081, China*
[d]*Institute of Physics, Chinese Academy of Sciences, Beijing 100190, China*
[e]*State Key Laboratory for Mesoscopic Physics and Frontiers Science Center for Nano-optoelectronics, School of Physics, Peking University, Beijing 100871, China*
[f]*National Center for Physics, Islamabad Pakistan.*

*aftab@cantab.net

View Article Online
DOI: 10.1039/D5MA01527H

Abstract

Palladium Diselenide ($PdSe_2$) exhibits unique anisotropic electronic behavior, high carrier mobility, and a layer-dependent indirect-to-direct bandgap transition, positioning it as a versatile material for next-generation 2D device architectures. In this work, we investigated the electrical properties; conduction and relaxation mechanisms of mechanically exfoliated $PdSe_2$ flakes. Raman spectroscopy and AFM were employed to confirm purity and thickness of the sample. Electrical characterizations including current–voltage (IV) measurements and complex impedance spectroscopy (CIS) were performed, revealing crucial information about charge carrier transport mechanisms, contact behavior, and resistive properties. For contact-limited conduction mechanisms, Schottky emission was investigated, and the thermionic emission model was employed to determine Schottky diode parameters, along with a re-evaluation of Richardson's constant. In bulk-limited conduction mechanisms, Poole–Frenkel (PF) emission was ascertained with a determination of the dielectric constant. To gain insight into relaxation mechanisms, complex impedance spectroscopy, complex dielectric permittivity, and complex modulus spectroscopy were conducted. A switching ratio of ~10^2 was achieved, indicating the suitability of $PdSe_2$ for applications in memory devices, neuromorphic computing, and sensing technologies.

Keywords: $PdSe_2$, IV characteristics, Schottky diode, Dielectric permittivity, Diode parameters

View Article Online
DOI: 10.1039/D5MA01527H

Highlights

- Raman spectroscopy and AFM confirmed the few-layered structure of $PdSe_2$ with a thickness of 4 nm leading to its semiconducting behavior.
- Temperature dependent I-V characteristics showed a switching ratio of ~10^2.
- The fitting of thermionic emission model led to the extraction of important Schottky diode parameters including Richardson coefficient, ideality factor and saturation current.
- Impedance spectroscopy was carried out to study the dielectric behavior and relaxation mechanisms.

DOI: 10.1039/D5MA01527H

Introduction

Recent advances in materials science have placed nanomaterials at the center stage of scientific and technological innovation with atomically thin 2D transition metal dichalcogenides (TMDCs) emerging as a major focus of current research. This attention has roots in the vast array of applications ranging from electronics and optoelectronics to sensing, catalysis and flexible devices. Unlike their bulk counterparts, TMDCs give access to highly tunable optical, electronic, chemical and mechanical properties (1, 2, 3). Among TMDCs, noble metal dichalcogenides (NMDCs), exhibit distinctive properties including thickness dependent electronic structure, remarkable air stability, unusual electronic phase transitions and in some cases even superconductivity (4). These materials comprise of chemical formula MX_2 where M is a Noble metal from group-10 (Pd, Pt) and X is a chalcogen (S, Se) (4).

Within the family of NMDCs, $PdSe_2$ draws attention as it is characterized by an orthorhombic phase resulting in an in-plane anisotropy and a layered, puckered pentagonal structure (5). The characteristics of these features are what make it exhibit a striking electronic band structure, such as a transition between semiconducting and metallic behavior with changing number of layers. Also, $PdSe_2$ has high air stability(5), tunable bandgap (6) and robust photo response properties(7), and thus is an appealing material to be incorporated in the infrared photodetectors, field-effect transistors, and gas sensors (8). Notably, $PdSe_2$ holds advantages over other group-10 dichalcogenides such as combining the durability of $PdTe_2$ under ambient exposure with the band tunability of $PtSe_2$, while maintaining thermodynamic stability that limits PdS_2. This unique combination places $PdSe_2$ as a more versatile and durable candidate for probing polarization phenomena and its integration into next-gen optoelectronic and sensing devices(9). However, the performance and reliability of these devices is strongly influenced by the underlying charge transport processes making it necessary to understand the conduction of charges across $PdSe_2$ layers for efficient and stable devices. This understanding can be achieved through detailed AC and DC analyses of conduction mechanisms. Despite the advances in $PdSe_2$ applications, simultaneous systematic studies of its AC and DC transport mechanisms remain relatively limited, highlighting the need for deeper investigation.

In this work, we address this gap by systematically investigating the conduction mechanisms in mechanically exfoliated nanoflakes of $PdSe_2$ with silver contacts by performing temperature dependent IV characteristics, complex impedance spectroscopy and complex dielectric permittivity analysis along with a brief complex modulus spectroscopy analysis. The observation

View Article Online
DOI: 10.1039/D5MA01527H

of non-linear behavior in the I-V plot of $PdSe_2$ was consistent with Schottky type contacts. The Schottky diode parameters were evaluated using thermionic emission model and a modified value of Richardson's coefficient for Ag/$PdSe_2$/Ag was re-evaluated. Analysis using Poole-Frenkel emission model enabled the extraction of dielectric permittivity constant of $PdSe_2$. The temperature and frequency dependence of the impedance in $PdSe_2$ was examined using Complex Impedance Spectroscopy (CIS) to elucidate the underlying charge transport and relaxation processes. Complex dielectric spectroscopy showed strong frequency and temperature dependence in permittivity (ε′), dielectric loss (ε″), and the complex modulus (M*), all of which provided evidence for localized carrier relaxation. This work not only expands the fundamental understanding of $PdSe_2$ but also highlights its potential as a robust candidate for future nano-electronic and optoelectronic applications.

Materials and methods

Bulk $PdSe_2$ crystals synthesized via chemical vapor transport (CVT) technique were acquired from a 6Carbon Technology, China. Interdigitated electrode arrays (IDAs) used for device fabrication were obtained from MicruX Technologies. Each IDA consisted of silver electrodes patterned on a glass substrate, arranged in an interdigitated comb-like configuration with individual finger dimensions of 10 μm × 10 μm.

$PdSe_2$ flakes with controlled thickness and lateral dimensions were mechanically exfoliated from the bulk crystals using thermal release tape (TRT). The exfoliation tape was gently pressed onto the target silicon substrate to ensure strong adhesion, followed by controlled thermal delamination, resulting in reliable transfer and adhesion of the exfoliated $PdSe_2$ flake onto the substrate surface.

The $PdSe_2$ flake with a thickness of approximately 4 nm was transferred onto a silver-contacted IDA using TRT and subjected to temperature-dependent I–V measurements in a cryogenic probe station of an Agilent 4156C semiconductor analyzer for a temperature range of 293 K – 393 K kept under control by liquid nitrogen. Moreover, AC transport measurements were made using an LCR meter 4980A in a frequency range of 200Hz to 2MHz for temperatures 293 K – 343 K with the temperature being controlled by liquid Nitrogen.

Results And Discussions

Mechanically exfoliated $PdSe_2$ flakes of desired thickness were then subjected to structural characterizations (figure 1). Raman spectroscopy was employed to investigate the structural and vibrational characteristics of the $PdSe_2$. Figure 1 (a) shows the Raman spectrum of bulk $PdSe_2$,

View Article Online
DOI: 10.1039/D5MA01527H

whereas Figure 1 (b) illustrates a distinct blueshift in the characteristic peaks, reflecting reduced interlayer coupling and stronger confinement effects showing a decrease in the number of layers. The few layered sample exhibited all 3 A (A_g^1, A_g^2, A_g^3) modes but only two B (B_{1g}^1, B_{1g}^2) modes. This is because B_{1g}^3 mode is very close to A_g^3 mode. Raman analysis validated the high phase purity of the synthesized $PdSe_2$, evidenced by the absence of any peaks attributed to impurity. The observed vibrational modes correspond closely to those reported for crystalline $PdSe_2$, confirming the material's structure and integrity (8). The sharpness and intensity of these peaks confirmed the crystalline nature of the sample and validated the successful transfer of a high-quality flake onto the substrate. The peaks observed in the lower frequency region at 75cm^{-1}, 100 cm^{-1} and 125 cm^{-1} are due to symmetry variations of $PdSe_2$. Absence of any background signals shows that the material is structurally intact and set for subsequent electrical characterizations.

For $PdSe_2$, the flake was exfoliated using TRT and placed onto Silicon wafers to perform AFM. Figure 1 (c) shows the visuals of the sample and figure 1 (d) shows the recorded deflection of the cantilever. A monolayer of $PdSe_2$ exhibits an average thickness of approximately 0.71 nm (10). The recorded value of the height profile obtained from atomic force microscopy (AFM) measurements for $PdSe_2$ shows that the thickness of the flake is ~4nm which is an equivalent of nearly 5 layers.

The schematic in figure 2 (a) depicts the device prepared as a flake is transferred onto a comb-like, 10 μm spaced, interdigitated silver electrodes of an IDA. Fig 2 (b) exhibits the I-V characteristic plots for the $PdSe_2$ flake with silver contacts in a temperature range of 293 K–393 K. The non-linear behavior of the curves becomes more pronounced upon an increase in temperature which is consistent with the semiconducting behavior. The switching ratio being ~10^2 makes it a reasonable candidate for analog synaptic elements in Neuromorphic devices, high-voltage sensors and high-voltage resistive switching devices (11, 12, 13).

In figure 3 (a), Schottky emission characteristics were analyzed by plotting ln(I) and $\sqrt{V}$ over the temperature range of 343 K–398 K. In Schottky emission, the current is governed by the thermionic emission of charge carriers across the metal-semiconductor junction, where the electrons are excited to energy levels high enough to surmount the potential barrier. The thermionic emission of electrons is expressed as (14):

View Article Online
DOI: 10.1039/D5MA01527H

$$I = AA^*T^2 \exp\left\{\frac{e\left(\varphi_b - \sqrt{\frac{eV}{4\pi\varepsilon_o\varepsilon_r Ad}}\right)}{k_\beta T}\right\} \quad (2)$$

Where A is the effective area, A^* is the Richardson's constant, V is the applied voltage, φ_b is the barrier height and d is the distance between the contacts, ε_o is the free space permittivity constant and ε_r is the dielectric permittivity. Applied voltages below 1.1 V result in nearly straight-line behavior in the plot which is a characteristic indication of conduction in this regime being governed primarily by Schottky emission.

The thermionic emission model fits the forward biased current in Schottky diode is illustrated in Fig 3 (b) and it expresses the forward biased current as (15):

$$I = I_s\left[exp\left(\frac{qV}{nk_\beta T}\right) - 1\right] \quad (3)$$

Where V denotes the applied voltage, n is the ideality factor, q is the electronic charge, k_β is the Boltzmann's constant, T is the temperature and I_s is the saturation current. The saturation current is the reverse bias leakage current due to the minority charge carriers crossing the junction. It is expressed as (15):

$$I_s = AA^*T^2 \exp\left(-\frac{q\varphi_b}{k_\beta T}\right) \quad (4)$$

The Schottky barrier height can be expressed by molding the above equation as follows:

$$\varphi_b = \frac{k_\beta T}{e}\ln\left(\frac{AA^*T^2}{I_s}\right) \quad (5)$$

The fitted curves helped to evaluate the values of saturation current and ideality factors for different temperatures using equation (3). These values are plotted against temperature in figure 3 (c). This plot helps gather Schottky diode parameters that are necessary to conclude possible device applications along with their performance. The ideality factor provides insight into the deviation of the device's behavior from that of an ideal diode. For an almost ideal case with low energy loss in semiconductors an ideality factor close to 1 is required. A value greater than 1 can be attributed to high field influencing the band. The ideality factor can be improved by taking measures towards improved charge carrier transport. The deduced values may allow for applications in heterojunction solar cells and photovoltaics.

View Article Online
DOI: 10.1039/D5MA01527H

Using these retrieved values, barrier height was calculated using equation (5) for different temperatures to be in the range of 0.128 eV – 0.150 eV. Height of the potential barrier governs the degree of charge carrier separation and associated energy losses. The nonlinear trend of barrier height φ_b is attributed to barrier inhomogeneities and is characteristic of multiple conduction mechanisms taking place at different points along the curve, which can be improved by performing strain engineering, doping etc. The temperature dependence of the barrier potential enables the device to serve not only as a sensor but also as a diagnostic platform for material characterization (16).

Equation 4 can also be modified to gain the value of Richardson's coefficient:

$$\ln\left(\frac{I_s}{T^2}\right) = \ln(AA^*) - \frac{q\varphi_b}{k_\beta T} \tag{6}$$

According to 6, upon linear fitting of $\ln(I_s/T^2)$ vs 1/T, the intercept of the plot should give Richardson's coefficient. The obtained value of the coefficient was significantly smaller than the theoretical expectation. The considerable discrepancy between the calculated and expected values can be attributed to barrier inhomogeneities(16). However, a corrected coefficient was determined by assuming a Gaussian distribution of the potential barrier heights, which introduces two new parameters: the mean barrier height (φ_{b0}) and the standard deviation (σ). These parameters are interrelated through the following expression:

$$\varphi_b = \varphi_{b0} - \frac{q\sigma^2}{2k_\beta T} \tag{7}$$

Here, φ_b is the experimentally determined value of potential barrier height whereas, φ_{b0} is to be measured using the expression above. When φ_b is plotted against 1/T the slope, it renders the value of σ, which came out to be 104.3 mV.

For corrected value of Richardson's constant, we used the Gaussian corrected equation (17):

$$\ln\left(\frac{I_s}{T^2}\right) - \left(\frac{q^2\sigma^2}{2\left(k_\beta T\right)^2}\right) = \ln(AA^*) - \frac{q\varphi_b}{k_\beta T} \tag{8}$$

Figure 3 (d) shows the plot between $(\ln I_s/T^2) - \left(q^2\sigma^2/2(k_\beta T)^2\right)$ vs 1/T is a straight line whose intercept was used to calculate the value of modified Richardson's coefficient. The intercept returned 421 $Acm^{-2}K^{-2}$ as modified Richardson's coefficient and 0.322 eV as the mean barrier height. Since these values are well within expected range, the Gaussian distribution being assumed was a success.

View Article Online
DOI: 10.1039/D5MA01527H

In figure 4, the plot between ln(G) vs $\sqrt{V}$ is illustrated for temperature range of 348 K–398 K for a voltage varying from 0 V–2 V. It depicts the Poole-Frenkel emission where electric field helps thermally weak, trapped charge carriers escape traps inside the potential valleys. PF emission obeys the following equation (18):

$$I \sim V\exp\left(\frac{\beta_{PF}\sqrt{V}-\varphi_{PF}}{k_\beta T}\right) \quad (9)$$

Where the β_{PF} is the lowering of potential barrier height, φ_{PF} denotes the potential barrier. Linear fit of the plots provides strong evidence of PF emission leading the conduction of charge carriers from 0 V–2 V. The slope of the plot provides the dielectric permittivity constant for the given temperature range according to expression (14):

$$S = \frac{\sqrt{\frac{q^3}{d\varepsilon_o\varepsilon_r\pi}}}{k_\beta T} \quad (10)$$

Where k_β is the Boltzmann constant, d is the electrode spacing, ε_o is the permittivity of free space, ε_r is the dielectric permittivity and q is the electronic charge. The inset of figure 4 depicts the change in dielectric constant ε_r with increase in temperature from 348K–398K. The average value of ε_r came to be around 8, which is well within the expected range. Dielectric constant of $PdSe_2$ is moderate in terms of polarizability. Therefore, moderate screening of the external field by the charge carriers is expected. The variation in dielectric constant is owed to thermally activated release of trapped charges, enhancing the polarization and screening ability of the material. The moderate yet tunable dielectric response highlights the potential of $PdSe_2$ for temperature sensitive applications like memristors and neuromorphic devices. With enhanced channeling abilities evident, $PdSe_2$ may also find applications in solar energy devices and memristors.

To delve deeper into the electrode and grain properties of $PdSe_2$ device, complex impedance spectroscopy was performed for a temperature range of 293 K–343 K at different frequencies. In figure 5 (a), Nyquist plots between the values of Z'' *and* Z' measured for the selected frequency domain are plotted. An equivalent circuit was designed using Z-view software and has been displayed in the inset of figure 5 (a). It consists of an R-CPE circuit showing crystalline nature of $PdSe_2$. The complex impedance of a system is given by(19):

$$Z^* = Z' - j\,Z'' \quad (11)$$

View Article Online
DOI: 10.1039/D5MA01527H

where Z′ and Z″ are the real and imaginary parts of the complex impedance which are then further individually expressed as (20):

$$Z' = \left[\frac{R}{1 + (\omega RC)^2}\right] \quad (12)$$

$$Z'' = \left[\frac{\omega CR^2}{1 + (\omega RC)^2}\right] \quad (13)$$

Where ω = angular frequency, R is the resistance and C is the capacitance of the device. The Nyquist plots exhibit a decrease in resistance as the temperature increases which is a characteristic of semiconductors with a negative temperature coefficient of resistance. Considering that $PdSe_2$ acts as a semiconductor when the number of layers is ~ 5 layers or less, it is consistent with the AFM values determined for this $PdSe_2$ device. The Nyquist plots were fitted using an equivalent circuit in Z-View, and the simulated curves showed excellent agreement with the experimental data (Table 1). As the temperature increases, the reduction in resistance is attributed to enhanced probability of thermally activated detrapping of charge carriers from defect states, increasing the free carrier concentration and effective mobility. The subsequent decline in total resistance with further temperature elevation clearly indicates a negative temperature coefficient, thereby reaffirming the semiconducting behaviour of the material.

Figure 5 (b) illustrates the decreasing trend of the real part of impedance (Z′) with increasing frequency over the temperature range of 293 K–343 K. At lower frequencies, Z′ exhibits negligible frequency dependence; however, as the frequency increases, a more pronounced decline is observed, and the Z′ values corresponding to different temperatures converge at higher frequencies. This behavior is attributed to the enhanced mobility of charge carriers and the resulting decrease in space-charge resistance, denoting improved electrical conduction in upper frequency domain. The inset of figure 5 (b) shows the varying trend of Z″ with the increase in frequency. The plot displays a rise in magnitude with increasing frequency, reaching a distinct peak, followed by a sharp decline that gradually converges as the frequency continues to increase. The decrease of Z″ is attributed mainly to the increased thermal activity. The peaks correspond to a certain value of frequency known as the relaxation frequency f_o. The values of f_o increase with the increase in temperature indicating an enhanced conduction of the localized charge carriers through hopping with the widening of peaks being a contribution from the temperature dependence of the relaxation mechanism.

Understanding the dielectric properties of a material is essential as it reveals the conduction mechanisms, polarization behavior, and dielectric relaxation processes that determine the device

View Article Online
DOI: 10.1039/D5MA01527H

performance (21). The polarization response of a material is inherently determined by its electronic, ionic, and interfacial characteristics, each of which shifts significantly with changes in frequency and temperature. The dielectric permittivity ε* has two parts, real and imaginary with the former usually referred to as the dielectric constant. It is expressed as (19):

$$\varepsilon^* = \varepsilon' - \mathrm{j}\,\varepsilon'' \tag{14}$$

The real part ε′ and the imaginary part ε″ are then further represented as:

$$\varepsilon' = \frac{t}{\omega A \varepsilon_o}\left(\frac{Z''}{Z'^2 + Z''^2}\right) \tag{15}$$

$$\varepsilon'' = \frac{t}{\omega A \varepsilon_o}\left(\frac{Z'}{Z'^2 + Z''^2}\right) \tag{16}$$

Where A is the cross-sectional area of the flake, t is its thickness, ε_o is the free space permittivity, Z′ and Z″ are the real and imaginary parts of impedance, respectively. In our case, the area is approximately $A = 1 \times 10^{-10}$ m and the thickness of the flake ~ 4nm. Using these values, the t/A ratio was calculated to be 40 m^{-1}.

In figure 5 (c), the plot between dielectric permittivity ε′ vs T for a temperature range of 293K-343K at specific frequencies shows a decrease in dielectric permittivity with the rise in frequency at all temperatures. This is because the interfacial polarizations are screened out at higher frequencies leaving behind only the ionic and electronic polarizations. The interfacial polarizations, key contributors, see an overall rise at lower frequencies due to better adaptation to field reversal but drop at higher values as per their inability to cope with the rapidly changing field. The contribution from other polarizations, however, becomes evident at higher frequencies but still the net polarization declines.

Figure 5 (d) depicts the change in dielectric loss $\tan\delta$ with temperature at specified frequencies. The dielectric loss is dependent on both parts of the dielectric permittivity and is represented as (20):

$$\tan\delta = \frac{\varepsilon''}{\varepsilon'} \tag{17}$$

Since, ε′ and ε″ are both parts of the same entity, they increase and decrease under the same conditions, the dielectric loss shows a similar trend. Therefore, as the temperature increases, the loss also increases due to enhanced thermal activity. This loss decreases with increase in frequency given the number of defects carrying charges also decreases (20).

View Article Online
DOI: 10.1039/D5MA01527H

In figure 6 (a), the change in calculated values of M' with changing M'' is demonstrated for a temperature range of 293 K-343 K. the two parameters are related by the following relation (19):

$$M^* = M' + j\,M'' \tag{18}$$

Where M^* is the dielectric complex modulus, M′ is the real part of the modulus related to energy storage and M″ is the imaginary part that reflects loss. These two are then further expressed as:

$$M' = \left(\frac{\varepsilon'}{\varepsilon'^2 + \varepsilon''^2}\right) \tag{19}$$

$$M'' = \left(\frac{\varepsilon''}{\varepsilon'^2 + \varepsilon''^2}\right) \tag{20}$$

Where ε' and ε'' are the real and imaginary parts of the dielectric constant. Complex modulus is often employed as an analytical tool to understand the relaxation mechanisms in a system. It helps understand the suppression of electrode polarization and enhances bulk relaxation. It gives a clearer insight into charge carrier dynamics and relaxation mechanisms.

Complex electrical modulus provides valuable information about the material's electrical response, revealing how varying polarization mechanisms behave under changing electric fields and temperatures. In figure 6 (a), a single semicircular arc is visible at all measured temperatures, exhibiting a slight movement toward higher M″ values as the temperature rises. This shift suggests that the modulus resistance decreases with rising temperature, which is in good agreement with previously reported findings (22). Figure 6 (b) illustrates the trend of M' with varying frequency for a temperature range of 293 K-343 K. At low frequencies, minimal electrode polarization occurs due to decreased effective restoring force to control charge carrier motion under the applied electric field, resulting in very small M' values (23) . As frequency increases, M' gradually rises and peaks at higher frequencies, signifying the presence of relaxation dynamics in the $PdSe_2$ flake throughout the studied range. The maximum M' value, however, diminishes with rising temperature. Since M' reflects the capacity of the material to store electrical energy, its reduction at elevated temperatures indicates improved charge carrier mobility within the system.

In figure 6 (b) inset, M'' is plotted against frequency for a temperature range of 293 K-343 K. A broad relaxation peak appears in M″ moving toward higher frequencies as temperature rises. This shift signifies a thermally activated relaxation process, where the frequency span under the peak represents the range of long-distance charge carrier mobility (24). The frequency at which a relation peak is observed is the characteristic frequency f_{max}. Below f_{max} the charge carriers can

View Article Online
DOI: 10.1039/D5MA01527H

easily cover the polarization length but greater than f_{max} the charge carriers cannot travel the polarization length, and the charge carriers are localized. As the temperature increases, the charge carriers gain energy and, thereby, they relax relatively slower while the peak shifts towards increasing frequency. This shift from long range mobility to short range mobility is evident in M'' plot (25).

Figure 6 (c) represents the response of complex modulus following scaling behavior by a plot of M''/ M''_{max} vs $\ln(f/f_{max})$. As the plotline climbs towards the peak, the charge carriers get restricted to their potential wells. The peak itself is evidence of transition of long-range movement to short-range. Moreover, the plot for different temperatures overlapping shows that the relaxation mechanisms are receiving equal thermal support (20).

In Figure 6 (d), the variation of Z'' and M'' with frequency provides valuable insight into the underlying relaxation mechanisms of the material. The two trendlines approach one another closely but do not overlap, signifying the coexistence of both localized relaxation processes and long-range conduction elements in $PdSe_2$ (26).

Conclusion

In this work, $PdSe_2$ flakes, exfoliated from bulk crystal using TRT and transferred onto the silver IDA contacts, were analyzed through temperature-dependent AC and DC transport mechanism between 293K and 398K. Both bulk-limited and contact-limited conduction mechanisms were observed. These include Schottky emission and PF emission. Schottky emission was investigated, and thermionic emission model was used to find the diode parameters and their trends with varying temperature. This device has shown a decrease in ideality factor, increase in saturation current and an inhomogeneous barrier height with an increase in temperature. The analysis of PF emission revealed the dielectric constant in the range of 7–10. Complex The investigation of complex impedance and modulus helped in determining the behavior of relaxation mechanisms and trend of dielectric permittivity in response to the changing polarity of the field. This study reinforces the suitability of $PdSe_2$ for high-performance nanoelectronics and optoelectronic applications and provides insights for optimizing device architectures. This work therefore contributes significantly to the broader understanding of Pd-based transition metal dichalcogenides and their role in next-gen 2D material technologies.

View Article Online
DOI: 10.1039/D5MA01527H

References

1. Tedstone AA, Lewis DJ, O'Brien P. Synthesis, Properties, and Applications of Transition Metal-Doped Layered Transition Metal Dichalcogenides. Chemistry of Materials. 2016;28(7):1965-74.

2. Wilson JA, Yoffe AD. The transition metal dichalcogenides discussion and interpretation of the observed optical, electrical and structural properties. Advances in Physics. 1969;18(73):193-335.

3. Manzeli S, Ovchinnikov D, Pasquier D, Yazyev OV, Kis A. 2D transition metal dichalcogenides. Nature Reviews Materials. 2017;2(8):17033.

4. Wang Y, Zhou L, Zhong M, Liu Y, Xiao S, He J. Two-dimensional noble transition-metal dichalcogenides for nanophotonics and optoelectronics: Status and prospects. Nano Research. 2022;15(4):3675-94.

5. Oyedele AD, Yang S, Liang L, Puretzky AA, Wang K, Zhang J, et al. PdSe2: Pentagonal Two-Dimensional Layers with High Air Stability for Electronics. Journal of the American Chemical Society. 2017;139(40):14090-7.

6. Leong Chow W, Yu P, Liu F, Hong J, Wang X, Zeng Q, et al. High Mobility 2D Palladium Diselenide Field-Effect Transistors with Tunable Ambipolar Characteristics. Advanced Materials. 2017;29(21):1602969-.

7. Long M, Wang Y, Wang P, Zhou X, Xia H, Luo C, et al. Palladium Diselenide Long-Wavelength Infrared Photodetector with High Sensitivity and Stability. ACS Nano. 2019;13(2):2511-9.

8. Wang Y, Pang J, Cheng Q, Han L, Li Y, Meng X, et al. Applications of 2D-Layered Palladium Diselenide and Its van der Waals Heterostructures in Electronics and Optoelectronics. Nano-Micro Letters. 2021;13(1).

9. Puretzky AA, Oyedele AD, Xiao K, Haglund AV, Sumpter BG, Mandrus D, et al. Anomalous interlayer vibrations in strongly coupled layered PdSe ₂. 2D Materials. 2018;5(3):035016.

10. Yu J, Kuang X, Li J, Zhong J, Zeng C, Cao L, et al. Giant nonlinear optical activity in two-dimensional palladium diselenide. Nature Communications. 2021;12(1):1-9.

11. Li Y, Loh L, Li S, Chen L, Li B, Bosman M. Anomalous resistive switching in memristors based on two-dimensional palladium diselenide using heterophase grain boundaries. Nature Electronics. 2021;4.

12. Park E, Seo JE, Noh G, Jo Y, Woo DY, Kim IS, et al. A pentagonal 2D layered PdSe₂-based synaptic device with a graphene floating gate. Journal of Materials Chemistry C. 2022;10(43):16536-45.

13. Di Bartolomeo A, Pelella A, Liu X, Miao F, Passacantando M, Giubileo F, et al. Pressure-Tunable Ambipolar Conduction and Hysteresis in Thin Palladium Diselenide Field Effect Transistors. Advanced Functional Materials. 2019;29(29):1902483.

14. Ali U, Abbas Q, Kazmi SMT, Bhatti MH, Sher F, Rafiq MA. Charge conduction in chalcopyrite CuFeS2 nanoflakes. Ceramics International. 2025;51(18):26098-106.

15. Kazmi SMT, Zahoor Z, Yusra NT, Bhatti MH, Afsar MF, Sher F, et al. Diode paremeters extraction and study of space charge limited current in (Ag, Au)/CoS2 Schottky diodes. Physica B: Condensed Matter. 2023;670.

16. Wong CPY, Troadec C, Wee ATS, Goh KEJ. Gaussian Thermionic Emission Model for Analysis of $\mathrm{Au}/{\mathrm{Mo}\mathrm{S}}_{2}$ Schottky-Barrier Devices. Physical Review Applied. 2020;14(5):054027.

17. Tataroğlu A, Pür FZ. The Richardson constant and barrier inhomogeneity at Au/Si3N4/n-Si (MIS) Schottky diodes. Physica Scripta. 2013;88(1):015801.

18. Abbas Q, Kazmi SMT, Li C, Xu X, Rafiq MA. Charge transport mechanisms of PbSnSe2 and observation of transition from direct to Fowler–Nordheim tunneling. RSC Advances. 2024;14(9):5812-6.

19. Joshi JH, Kanchan DK, Joshi MJ, Jethva HO, Parikh KD. Dielectric relaxation, complex impedance and modulus spectroscopic studies of mix phase rod like cobalt sulfide nanoparticles. Materials Research Bulletin. 2017;93:63-73.

20. Kazmi SMT, Abbas Q, Li C, Xu X, Rafiq MA. Temperature and frequency dependence of conductivity, density of states, and dielectric permittivity of ternary metal chalcogenide PbSnSe2 flake. Ceramics International. 2024;50(14):25763-70.

21. Mohamed CB, Karoui K, Saidi S, Guidara K, Rhaiem AB. Electrical properties, phase transitions and conduction mechanisms of the [(C2H5)NH3]2CdCl4 compound. Physica B: Condensed Matter. 2014;451:87-95.

22. Wang X, Zhuang J, Peng Q, Li Y. A general strategy for nanocrystal synthesis. Nature. 2005;437(7055):121-4.

23. Macedo P B. The role of ionic diffusion in polarisation in vitreous ionic conductors. Phys Chem Glasses. 1972;13:171-9.

24. Chanmal CV, Jog JP. Dielectric relaxations in PVDF/BaTiO3 nanocomposites. Express Polym Lett. 2008;2:294-301.

25. Ben Nasr W, Mahmoud A, Boschini F, Ben Rhaiem A. Optical and AC conductivity studies on Li2-xRbx MoO4 (x = 0, 0.5, 1) compounds. Journal of Alloys and Compounds. 2019;788:522-32.

26. Imran Z, Rafiq MA, Ahmad M, Rasool K, Batool SS, Hasan MM. Temperature dependent transport and dielectric properties of cadmium titanate nanofiber mats. AIP Advances. 2013;3(3).

View Article Online
DOI: 10.1039/D5MA01527H

Figure 1

View Article Online
DOI: 10.1039/D5MA01527H

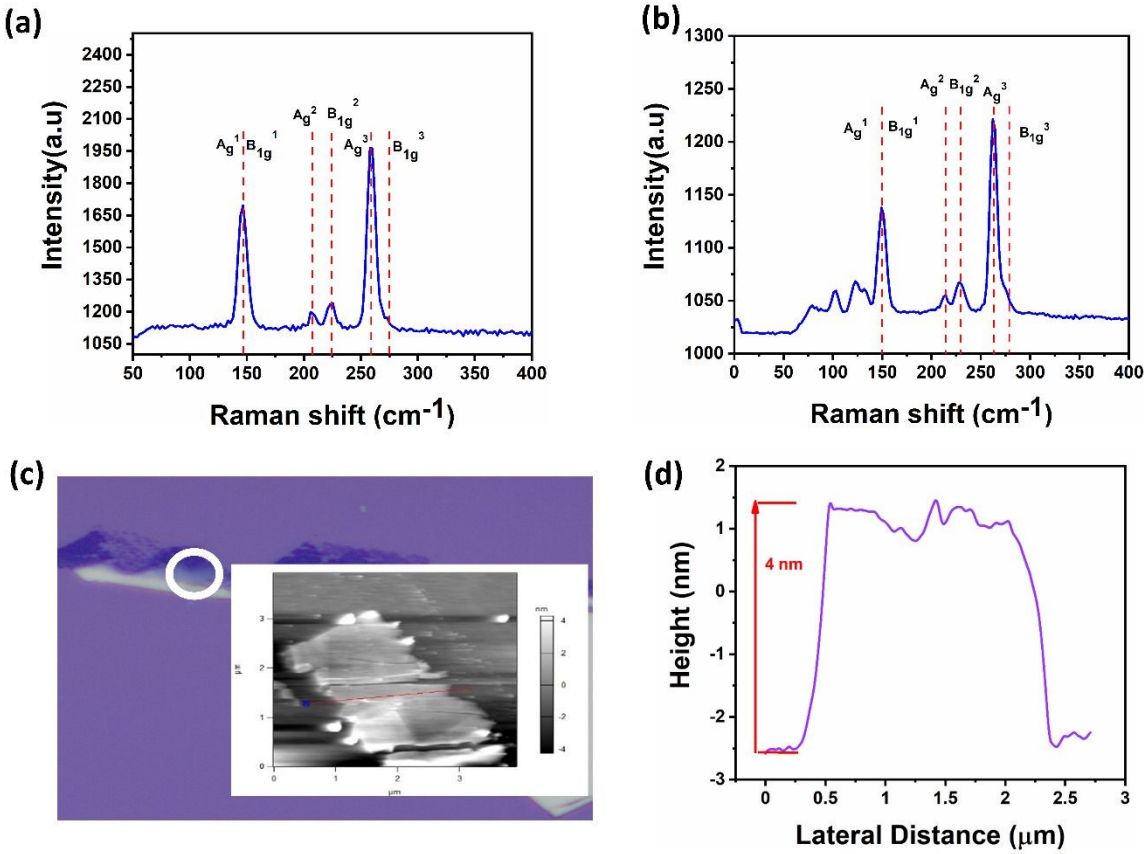

Figure 1: (a) Raman spectrum of the bulk $PdSe_2$ showing the characteristic vibrational modes corresponding to bulk phase (b) RAMAN spectrum of the mechanically exfoliated few-layered $PdSe_2$ flake confirming layer reduction by via blue shifts. (c) AFM image showing the magnified region of the exfoliated $PdSe_2$ flake used for thickness measurement. The selected area highlights the region analyzed to determine the layer thickness of the flake. (d) AFM height profile of the exfoliated few-layered $PdSe_2$ flake on a Si/SiO_2 substrate.

Figure 2

View Article Online
DOI: 10.1039/D5MA01527H

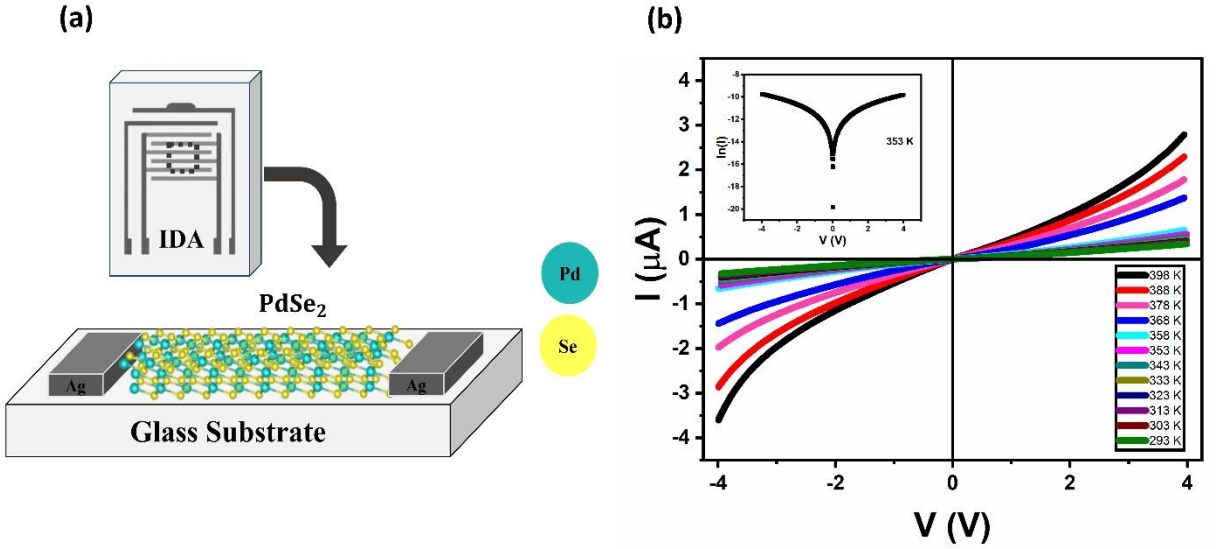

Figure 2: (a) Schematic of $PdSe_2$ flakes on IDA with silver contacts 10 μm apart on a glass substrate. (b) Temperature-dependent IV characteristics of $PdSe_2$ flakes in the temperature range of 293 K–398 K show negative temperature coefficient.

Figure 3

View Article Online
DOI: 10.1039/D5MA01527H

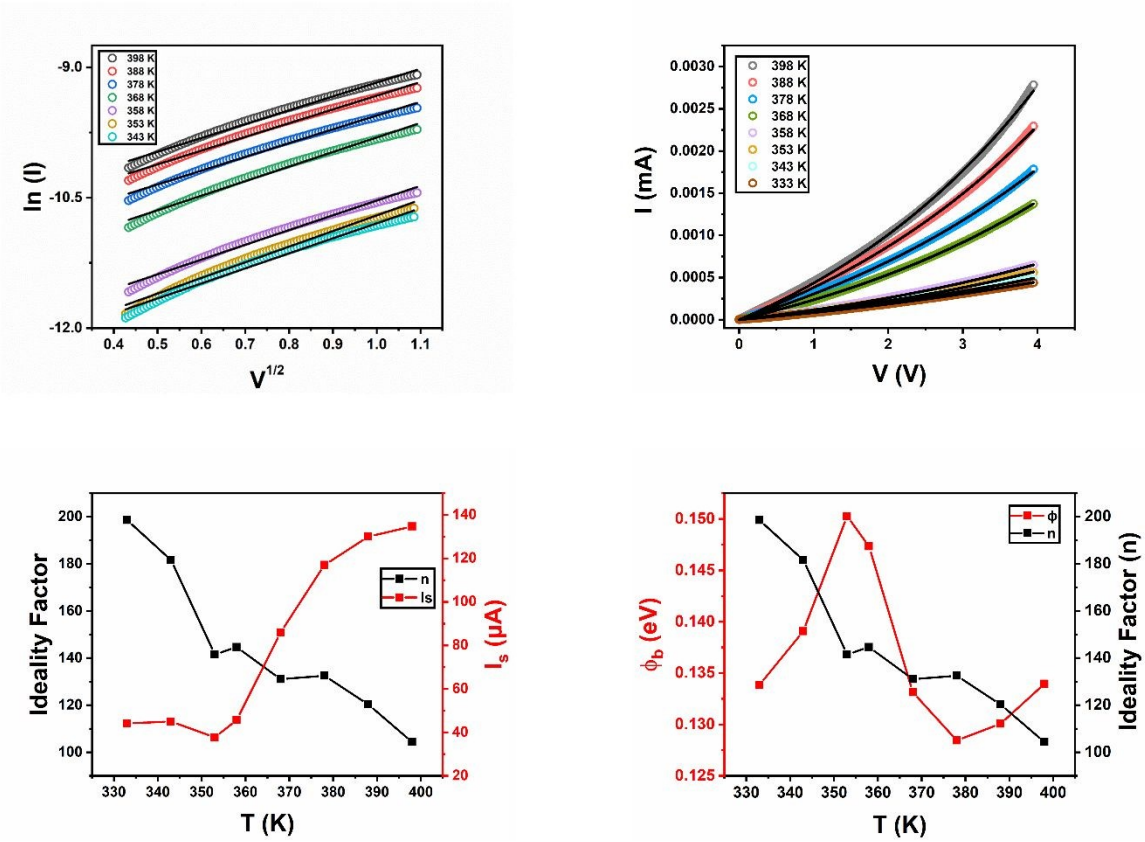

Figure 3: (a) Plot between $ln(I)$ *vs* $V^{1/2}$ for Schottky emission fitting (b) Equation fitting of thermionic emission model (c) Variation of ideality factor and saturation current with temperature (d) Modified Richardson plot according to Gaussian distribution of the barrier heights for $PdSe_2$.

Figure 4

View Article Online
DOI: 10.1039/D5MA01527H

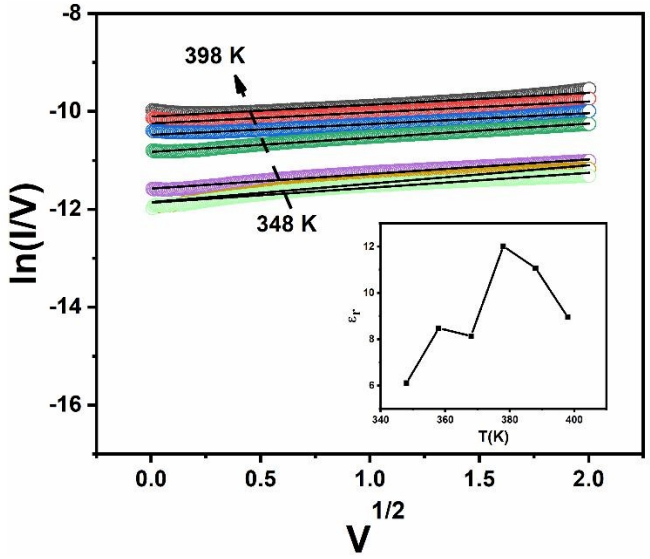

Figure 4: *ln(I/V) vs.* $V^{1/2}$ for the Poole–Frenkel emission at temperatures 348 K-398 K; the inset shows the variation of dielectric constant.

Figure 5

View Article Online
DOI: 10.1039/D5MA01527H

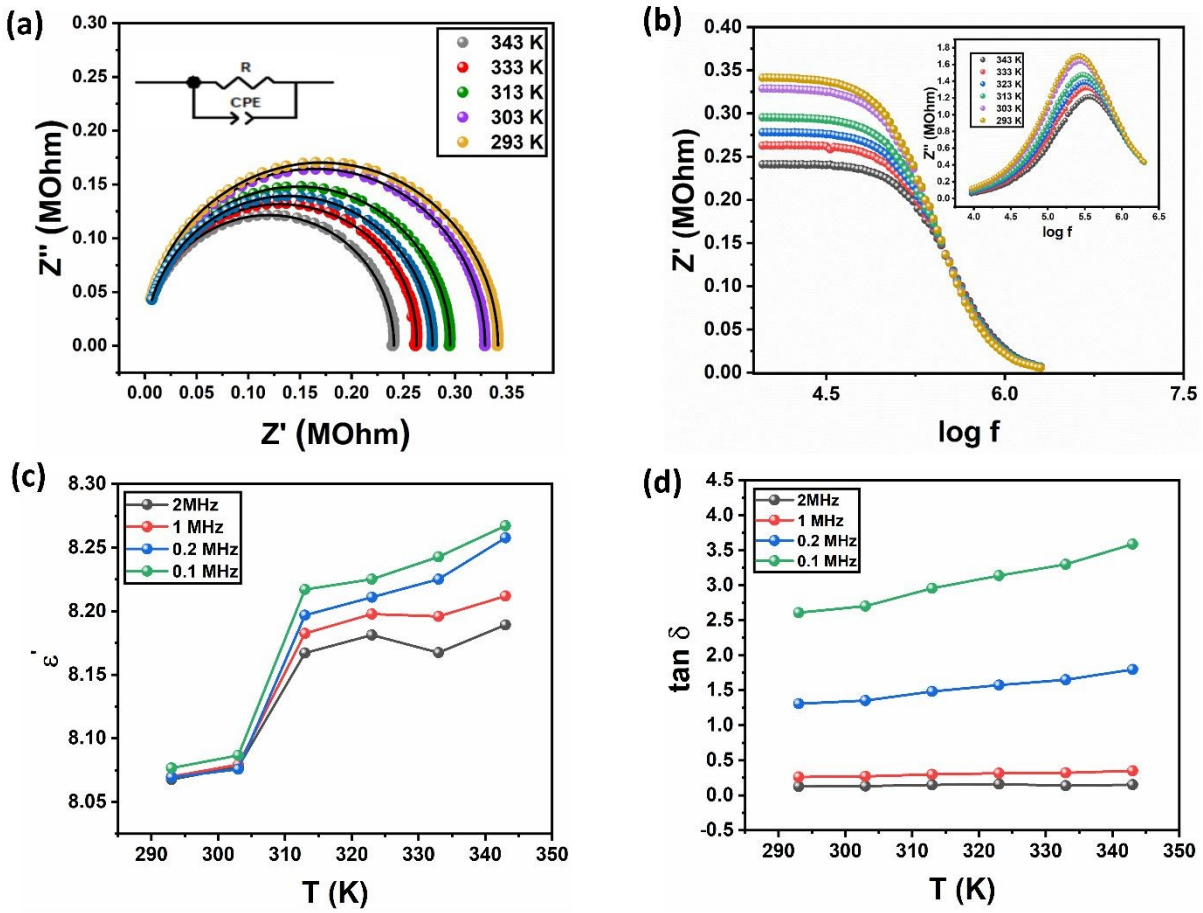

Figure 5: (a) The Nyquist plots of $PdSe_2$ flake in the temperature range of 293 K–343 K along with the circuit fittings and the inset shows the equivalent circuit containing a resistance (R) and a constant phase element (CPE) connected in parallel. (b) The variation of Z' with frequency in the temperature range of 293 K–343 K; the inset exhibits the behavior of Z'' with frequency in the temperature range of 293 K–343 K. (c) The trend of ε′ with temperature at specific values of frequency. (d) The trend of tan δ with temperature at specific values of frequency.

Figure 6

View Article Online
DOI: 10.1039/D5MA01527H

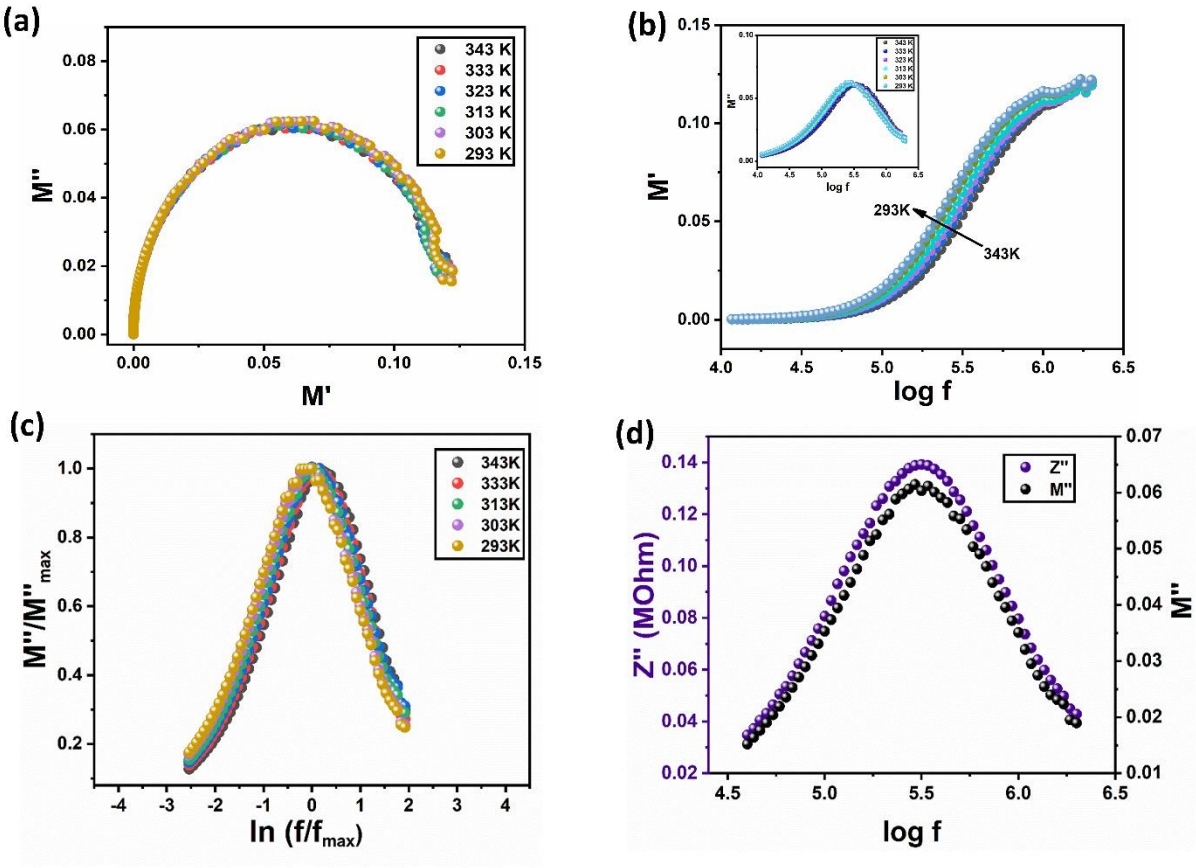

Figure 6: (a) The M' vs M'' plots of mechanically exfoliated $PdSe_2$ flake in the studied temperature range. (b) The behavior of M' with frequency at different temperatures; the inset shows the behavior of M'' with frequency at different temperatures. (c) M''/M''_{max} vs $ln\,(f/f_{max})$ plot at specific values of temperature. (d) The comparison between Z'' and M'' with frequency at a specific temperature of 323 K.

Table 1

View Article Online
DOI: 10.1039/D5MA01527H

Table 1: The Z-view fitted parameters of the model (R-CPE) at specific temperature values.

Temperature (K)	Resistance R (Ohms)	Capacitance C (pF)	n
343	2.418×10^5	1.847	1.0
333	2.634×10^5	1.833	0.9
323	2.783×10^5	1.825	0.87
313	2.955×10^5	1.821	0.92
303	3.291×10^5	1.795	0.88
293	3.413×10^5	1.779	0.79

View Article Online
DOI: 10.1039/D5MA01527H

Data Availability Statement

The data that support the findings of this study are available from the corresponding author upon reasonable request.